Automatic grain boundary detection and grain size analysis using polarization micrographs or orientation images

Renée Heilbronner*

Department of Earth Sciences and Department of Scientific Photography, Basel University, Basel, Switzerland

Received 9 January 1999; accepted 7 February 2000

Abstract

A simple procedure for creating grain boundary maps from petrographic thin sections, termed the Lazy Grain Boundary (LGB) method, has been devised. It is based on a set of macro commands programmed for NIH Image, a public domain image processing software. The grain boundary detection is based on gradient filtering. The procedure makes use of multiple input images: sets of regular polarized micrographs or—where possible—orientation/misorientation images. On each image of a given input set, only the most significant grain boundaries are detected and by combining those, a single grain boundary map is obtained. Image models and criteria for grain boundary identification are discussed briefly. The principal aim of the LGB method is to facilitate the production of large grain boundary maps (containing several thousand cross-sectional areas) to provide statistically valid samples for grain size analysis.

A section of Black Hills quartzite was used to test the LGB method. Five different input sets were prepared and used for automatic LGB analysis. One set was additionally used for an interactive analysis and for a manual tracing. From all seven grain boundary maps, the 2- and 3-D grain size distributions were calculated. The results are compared and the different image sets and procedures are rated for precision, over- and undersegmentation and speed of preparation. © 2000 Elsevier Science Ltd. All rights reserved.

1. Introduction

In many fields of microstructural analysis, grain size plays an important role. For example, in paleopiezometry the recrystallized grain size is related to the flow stress during deformation (e.g. Twiss, 1977; Etheridge and Wilkie, 1981), in igneous petrology the grain size is related to the crystallization history (Marsh, 1988; Cashman and Ferry, 1988), and in sedimentology, grain size is related to the environment of deposition (e.g. Pettijohn et al., 1987). Because of the obvious need for grain size analysis, many different techniques have been proposed for measuring average grain size or grain size distributions in two dimensions (e.g. Underwood, 1970; Marsh, 1988).

As pointed out in a previous publication (Heilbronner and Bruhn, 1998), the volume weighted distribution of radii of (three-dimensional) spheres, $V(R)$, conveys more physically relevant information than the numerical distribution of (two-dimensional) radii of sectional circles, $h(r)$, or the average grain size as obtained by the linear intercept method. However, the determination of the $V(R)$ distribution from the $h(r)$ histogram requires very large data sets of grain boundary outlines, so-called grain boundary maps, which are very tedious and time consuming to prepare manually. This paper describes a new and relatively simple method, the 'Lazy Grain Boundary' (LGB) method to automatically prepare (large) grain boundary maps from which the 3-D grain size distribution can be derived.

Since the effects of grain shape are not considered in

---

* Corresponding author. Geologisches Institut, Bernoullistr. 32, CH-4056 Basel, Switzerland. http://www.unibas.ch/earth/GPI/micro/micro.html.

E-mail address: renee.heilbronner@unibas.ch (R. Heilbronner).

the grain size analysis, the fine details of local grain boundary curvature etc. are not given much attention: the emphasis of the LGB method is on obtaining large data sets of approximately correct cross-sectional areas rather than preparing small sets of very precisely digitized grain shapes. A typical feature of the LGB method is to use more than one micrograph or orientation image of a given sampling site as a basis for segmentation (edge detection). In this manner, many artefacts associated with scratches or low contrast boundaries are avoided, and the detected grain boundaries can be considered significant.

In this paper, a thin section of Black Hills quartzite (BHQ) is used to demonstrate the LGB method. Two sets of regular polarization micrographs were prepared. Since the mineral is uniaxial it was possible to additionally calculate various optical orientation and misorientation images by the computer-integrated polarization microscopy (CIP) method (Heilbronner, 1997; Panozzo Heilbronner and Pauli, 1993); from these, three additional input sets were prepared. Although it will be shown that a set of misorientation images yields the best grain boundary map, this does not imply that orientation imaging is a prerequisite for successful grain boundary detection by the LGB method.

2. The Lazy Grain Boundary method

The aim of the LGB method (Heilbronner, 1999) is to identify grain boundaries in a crystalline aggregate, and to represent them as outlines, i.e. as a grain boundary map. It involves the preparation of a set of input images, optical micrographs or orientation images, and the application of a series of image processing routines from the LGB macro, which is represented schematically in Table 1. Typical input images that can be used for the LGB method will be discussed briefly.

2.1. The input images

A polished, uncovered thin section of BHQ, a 100% pure quartzite, was used. Fig. 1 shows that on polarization photomicrographs and on orientation or misorientation images, different grey-values indicate different c-axis orientations. However, the reverse is not necessarily true: identical grey values need not indicate identical c-axis orientations. For a fixed relative orientation of the thin section with respect to the crossed polarizers, two adjacent grains may have the same grey value and still have different c-axes orientations as shown, for example, by the grains marked by arrows in Fig. 1(C and D). Grey value contrasts at grain boundaries may appear and disappear depending

on the rotation of the microscope table. This is why, in the image analysis procedure proposed here, a series of images will be analysed, and why the segmentation is not performed on a single image but compiled from a set of images, as shown schematically in Fig. 2.
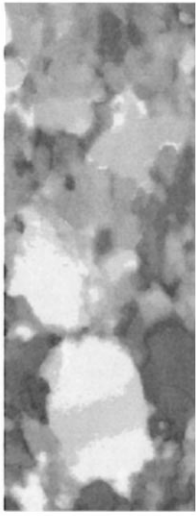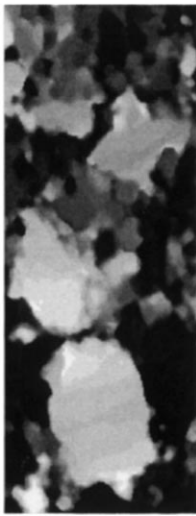
2.2. Grain boundary detection
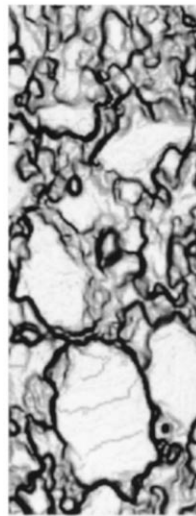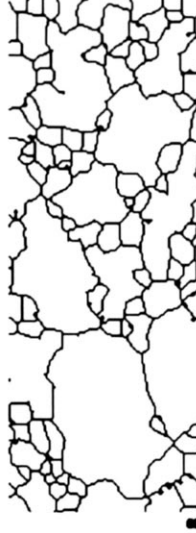
In image processing terms, grain boundary detection is edge detection. General image processing algorithms for automated edge detection are difficult to design (for an introduction to digital image analysis, see e.g. Rosenfeld and Kak, 1976; Pratt, 1978; Gonzalez and Wintz, 1987). This is mainly due to the problem of finding suitable image models. The image model is a concept of how the edges, i.e. grain boundaries are represented in the image. The image model dictates which image processing algorithm(s) should be used for the segmentation of the image, i.e. for the identification of the grain boundaries. For example, if the grain boundaries appear as black outlines, forming a rim of black pixels around each grain (0 = black, 255 = white), the appropriate image model defines as grain boundary every pixel with a grey value below a certain threshold value; and the grain boundaries are isolated by thresholding or grey-level-slicing. If the grain boundaries appear as a change of grey value from one grain to the next, the appropriate image model defines as grain boundary those pixels where large changes of grey value occur; and the grain boundaries are found by gradient filtering. Because of the prevalence of grain boundaries for which the latter image model is appropriate, the LGB method is based upon gradient filtering as a means for edge, i.e. grain boundary detection.

2.3. The grain boundary criterion

Gradient filtering does not return a bitmap, but a half-tone image of more or less significant and more or less coherent edges. We are faced with two problems (1) can we convert the grey values to angular differences?, and (2) where is the significance level that discriminates grain boundaries from noise? With respect to this, the CIP images present no problem since they are true and calibrated orientation images, and a number of concepts for minimum misorientation angles have been developed in the literature (see Trimby et al., 1998 and references therein). For polarization micrographs, however, the conversion to angles is not generally possible—only the circular polarization image can be calibrated—and minimum criteria are even more difficult to devise.

Prescribing a minimum angle of (c-axis) misorientation, the true orientation gradient image (set 5, Fig. 2) can be thresholded easily. However, the problem with

Table 1
Schematic representation of image segmentation by the Lazy Grain Boundary method using the LGB macro for NIH Image

Stack of input images

3 misorientation images:
misE (from East),
misH (from up),
misN (from North)
(detail of last slice of stack)

Lazy grain boundaries:
c, enhance contrast of stack;
u, median filter stack

Lazy grain boundaries:
o, sobel filter stack
(edge detection)

Lazy grain boundaries:
g, adaptive threshold stack
(threshold = mean of
histogram);
u, median filter stack

Lazy grain boundaries:
z, maximum of stack

→ stack reduced to one
image

Lazy grain bundaries:
t, thicken lines

Lazy grain boundaries:
j, skeleton image

Lazy grain boundaries:
i, prune image*
(*cut off unconnected lines)

Lazy grain boundaries:
t j i t j i, twice the following:
thicken outlines, skeletonize
image,
prune image
→ outlines

Lazy grain boundaries:
5, trim off a rim of 6 pixels
width;
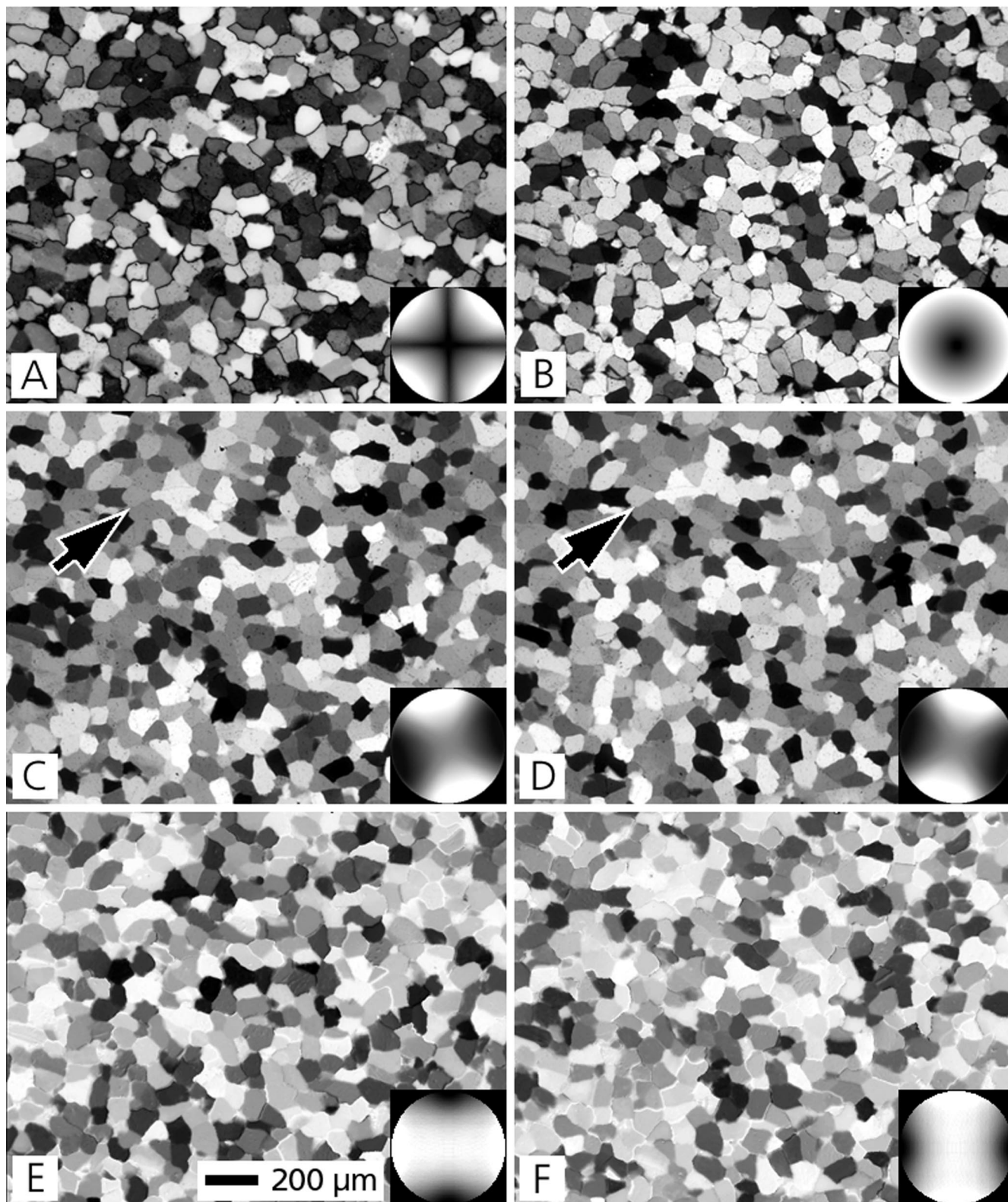**t**, thicken outlines; **y**,
invert image
→ areas

Fig. 1. Photomicrographs (A–D) and misorientation images (E and F) of undeformed Black Hills quartzite with the corresponding look-up table (LUT) shown at lower right. The LUTs are upper hemisphere stereographic projections of brightness as function of *c*-axis orientation: for example, in A, grains with flat-lying, diagonally striking *c*-axes appear bright, those with vertical or horizontal *c*-axes, appear dark, etc. Scale bar applies to all figures. Photomicrographs: A—crossed polarizers; B—circular polarization (brightness depends on inclination of *c*-axis with respect to section plane); C—crossed polarizers and λ-plate, rotated 30° clockwise, colour image filtered through narrow-band interference filter (transmission 661.2 ± 4.6 nm); D—same as C, except that polarizers and λ-plate are rotated 60° clockwise. In C and D, the interference filter renders first order yellow bright and first order blue dark. Misorientation images: E—angular difference with respect to North–South axis; F—with respect to East–West axis (grey values correspond to angle of misorientation: black = 0°, white = 90°).

POLARIZATION MICROGRAPHS
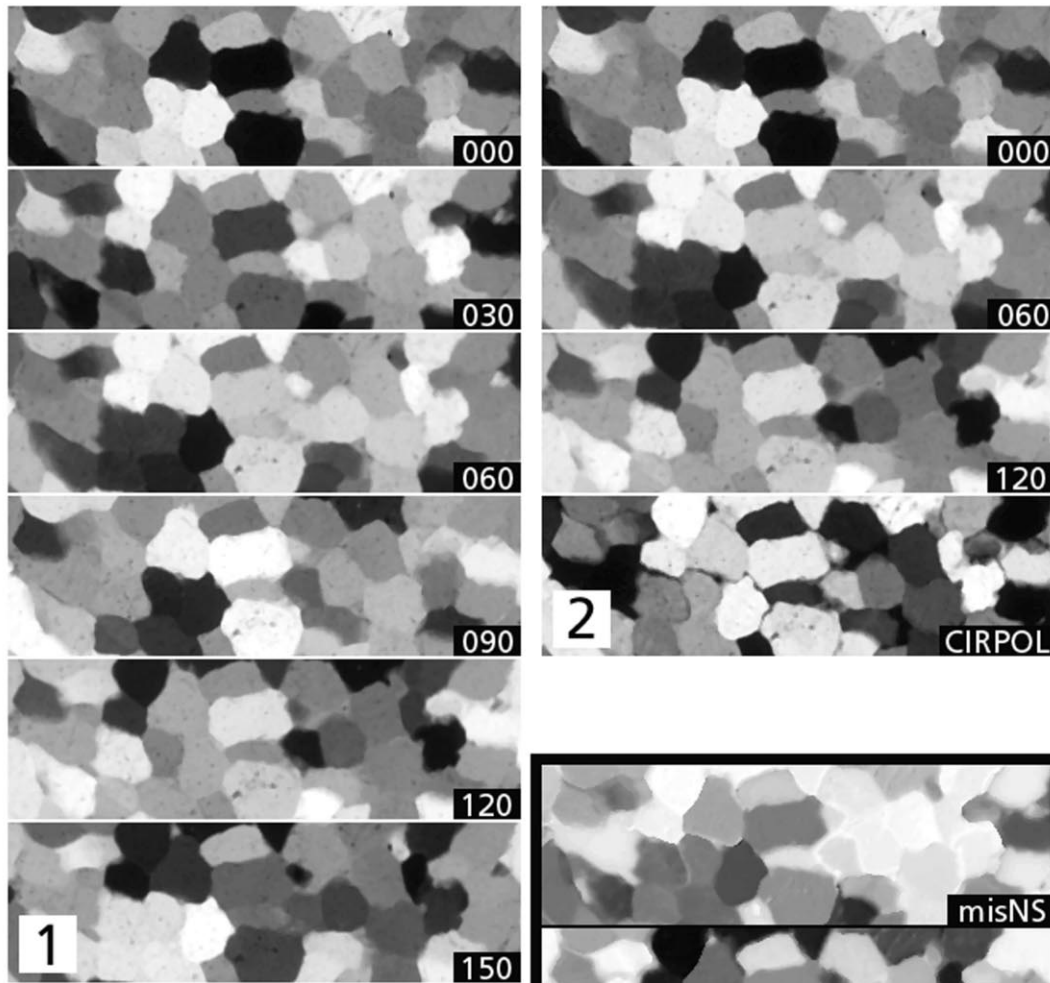
ORIENTATION / MISORIENTATION IMAGES
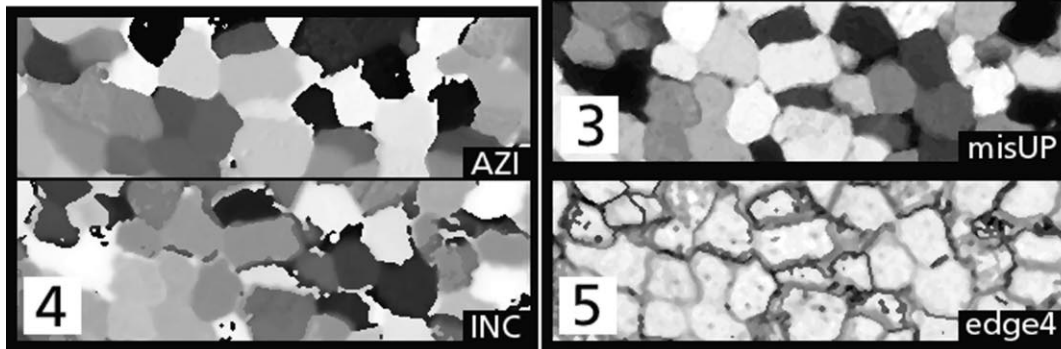
Fig. 2. Schematic representation of five sets of input images for the Lazy Grain Boundary detection method. Top: photomicrographs, bottom, black background: CIP calculated orientation and misorientation images. Microstructure is a detail of Fig. 1: set 1—Six polarization micrographs: six images with crossed polarizers and λ-plate rotated 0°, 30°, 60°, 90°, 120°, 150°; interference filter as in Fig. 1(C and D); set 2—Four polarization micrographs: three images with crossed polarizers and λ-plate rotated 0°, 60°, 120°, and 1 circular polarization image; interference filter as in Fig. 1(C and D); set 3—Three misorientation images: misorientation image with respect to North–South axis (misNS), East–West axis (misEW) and axis perpendicular to image plane (misUP); set 4—Two orientation images: azimuth image, inclination image (median-filtered); set 5—One orientation gradient image: angular difference between orientation of a pixel and that of its four neighbours (median-filtered).

true gradient images is that they tend to be very noisy; many erroneous grain boundaries appear and severe preprocessing and/or structural filtering is necessary to eliminate the noise. A much better result is obtained if three misorientation images (set 3, Fig. 2) are gradient-filtered and the most significant grain boundaries are compiled into one image. 'Significant' means that (a) there has to be a minimum gradient, either based on the mean or mode of the grey value histogram of the gradient image or according to a minimum angle criterion, and (b) that there has to be a connected region of grain boundary pixels which is large enough to 'survive' the structural and median filtering process. Both single pixels of high gradient values and large regions of low gradient values are not 'significant'.

2.4. The procedure

NIH Image (for Macintosh, National Institute of Health, 1999) or its equivalent, Scion Image (for Windows, Scion Corporation, 1999), is started; and the LGB macro is loaded. The LGB macro consists of five parts: part 1 where the images of the stack are pre-processed, part 2 where the images of the stack are segmented individually, part 3 where the segmented images of the stack are combined into one image, part 4 where further segmentation and skeletonization is performed, and part 5 where the fully segmented grain boundary map is post-processed to render it suitable for grain-size analysis. The end result of the LGB procedure is a bitmap of grain boundary outlines.

The LGB method uses monochrome or grey scale images as input; the images are opened and combined to a stack. It is also possible to start with a single input image; in this case, the entry point for segmentation is part 3 of the LGB macro. A detailed manual for the application of the LGB macro (Heilbronner, 1999) can be found on the authors web-site. Table 1 shows a possible choice of steps that can be used to perform a segmentation of an input stack which consists of three misorientation images. The sequence shown in Table 1 was established by trial and error; it is the one best suited to segment Black Hills quartzite.

One of the most critical factors affecting the outcome of the segmentation is the choice of the thresholding level in part 2. The LGB macro offers three options for thresholding the gradient image in function of the grey value histogram: mean, mode or mixed level [(mode + mean)/2]. Usually, the histogram of the gradient image is strongly positively skewed with a mode at very low gradients. Therefore, the mean, being at higher levels, presents a more discriminating threshold than the mode. It is also possible to select a numerical value or to use the regular thresholding tool from the Options menu of NIH Image/Scion Image.

Another important factor is the sequence of thicken-

ing and thinning adopted during structural filtering in part 4. The first step after compiling the slides of the stack into one image is critical. If a thickening step is executed first, many outlines and holes are closed. For very fine-grained materials, this may result in too much 'closing', i.e. loss of grains. If the first step is to skeletonize the image, too many holes may remain open, and too many grains may be the result.

3. Grain size analysis

After segmentation, the grain boundary map is saved. The NIH Image/Scion Image Analyse menu is used for measuring the cross-sectional areas of the grains. The scaling of the images is set to pixels, the particles are analysed and the resulting measurement file, listing the pixel values of the cross-sectional areas and of the perimeters, is exported and saved.

A spread-sheet program such as Kaleidagraph (Abelbeck Software, 1994) is used to calculate the equivalent radii of the cross-sectional areas. The corrected areas (see Heilbronner and Bruhn, 1998) are scaled and used to calculate the equivalent radius (= radius of circle with same area as the cross-sectional area). The equivalent radii are grouped into histograms of 20 classes where the bins are delimited by their upper bound. The program StripStar (Heilbronner, 1998) is used to calculate the parent distributions of spheres [$V(R)$ = volume density of radii of spheres] from the histograms of equivalent radii [$h(r)$ = number density of radii of circles]. Using Kaleidagraph again, the resulting histograms are plotted.

4. Grain boundary detection of different sets of input images

Five sets of input images (shown schematically in Fig. 2) were analysed. Sets 1 and 2 can be obtained directly through polarizing microscopy. Sets 3, 4 and 5 are orientation and misorientation images calculated by the CIP method (Heilbronner, 1997).

4.1. Manual and interactive grain boundary detection

On a micrograph the grain boundaries were traced manually as follows: three 780 × 620 misorientation images (with respect to North–South, East–West and Up) were copied into three layers of a Photoshop image, and the tracing was generated in a fourth transparent layer using the pencil tool. The misorientation images were turned on and off in turn to retrieve all significant grain boundaries. In case of doubt additional micrographs were consulted. The tracing required approximately four hours and returned approximately 500

grains. Note that, as a general rule, 500 grains are not sufficient for grain size analysis, but in view of the time needed for manual tracing, and since this exercise was undertaken to test the quality of the LGB method, 500 grains were considered sufficient.

A second grain boundary map was obtained by an interactive procedure where the LGB method was used in a supervised mode: broken grain boundaries were re-joined and closed grains were re-opened by hand on the basis of visual interpretation. The same set of misorientation images that were used for the manual tracing were opened in NIH Image/Scion Image and combined into a stack. The LGB method was started but not carried through in an automatic fashion. Instead, at various steps of the procedure, corrections were applied using the pencil tool or the block eraser. This procedure required approximately one hour and returned a grain boundary map that matches the manual tracing very closely both in number, size and shape of grains.

4.2. Fully automatic grain boundary detection

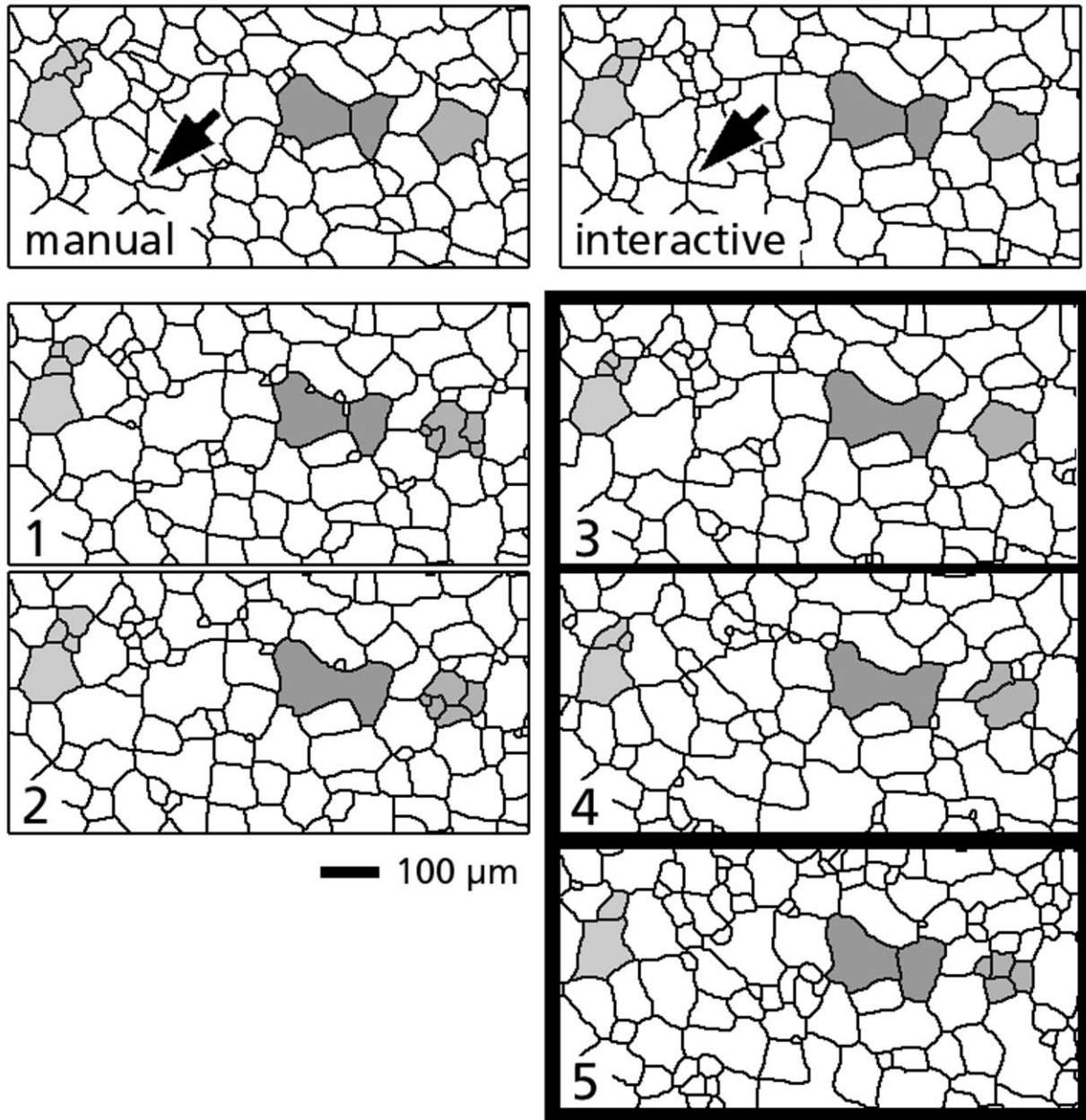Sets 1–4 were subjected to the entire LGB procedure

Fig. 3. Details of grain boundary maps derived by manual tracing (manual), supervised grain boundary detection (interactive) and automatic grain boundary detection (sets 1–5). Grain boundary maps 1–5 correspond to image sets 1–5 of Fig. 2. Three regions are highlighted, arrows point to segmentation artefacts, see text for discussion.

Table 2
Comparison of the quality of grain boundary detection derived for different sets of images using different procedures[a]

Sets	Input images	Procedure / Software	Grain boundary match compared to manual			Matched:non-matched (%)	Ranking	Matched:total gb (%)	Ranking	Detected grains / Total number	Ranking	Time / Min.	Ranking	Rating / Final Ranking
			Matched (pixels)	Non-matched (pixels)	Total grain boundary (pixels)									
1	2	3	4	5	6	7		8		9		10		11
Manual	Three principal misorientation images: **misNS/EW/Up**	Manual tracing: photoshop layers	43 554	0	43 554	∞		100		509		240		11
Interactive	Three principal misorientation images: **misNS/EW/Up**	NIH image: LGB macro interactive	20 386	23 168	41 109	88	2	50	1	495	1	60	3	2
1	Six rotation images (30° interval): **030–060...150**	NIH image: LGB macro standard procedure	19 631	23 923	42 079	82	3	47	2	525	2	2	1	3
2	Three rotation images (60° interval), one circular polarization image: **000–060–120–cirpol**	NIH image: LGB macro standard procedure	18 087	25 467	42 590	71	4	42	3	535	4	2	1	4
3	Three principal misorientation images: **misNS/EW/Up**	NIH image: LGB macro standard procedure	20 803	22 751	41 813	91	1	50	1	532	3	2	1	1
4	Azimuth and inclination image (noise removed): **azi/incp**	NIH image: LGB macro standard procedure	17 233	26 321	44 374	65	5	39	4	662	5	2	1	5
5	One orientation gradient image (four neighbours): **edge 4**	NIH image: part 1: preprocessing, part 2: LGB macro	15 894	27 660	48 272	57	6	33	5	780	6	15	2	6

[a] 1 Name of data set. 2 Type of images used as input sets. 3 Procedure and software used. 4 Number of detected boundary pixels that coincide with manual tracing. 5 Number of pixels on manual grain boundaries that are not matched by detected boundary pixels. 6 Total number of detected grain boundary pixels. 7 Ratio of matched vs. non-matched grain boundary pixels in %. 8 Ratio of matched pixels vs. total number of detected grain boundary pixels in %. 9 Total number of detected grains. 10 Time necessary for various procedures; time for preparation of input images is not included. 7–10 Ranking for each criterion is included in table. 11 The final rating is obtained from the added rankings of columns 7–10.

(part 1–5 of the LGB macro) in a completely automatic way. After a few trials the sequence of key strokes shown in Table 1 was adopted for all sets. Steps 7–9 were repeated three times. Set 5, being a single image, was pre-processed separately (interactive thickening and thresholding) and only subjected to part 4 and 5 of the LGB macro.

For comparison, a detail of all seven grain boundary maps is shown in Fig. 3. A well known problem in image segmentation is over- and undersegmentation: either a grain boundary which exists is not detected or a grain boundary is detected where none exists (compare highlighted regions in Fig. 3). A further problem is the occurrence of artefacts: the shape of grain boundaries is related to the thinning algorithm itself and not to the actual shape of the grain boundary. Each skeletonization has its own characteristics, junctions of four diagonal lines are very typical artefacts (Fig. 3, arrows). There is no universal solution to this problem. For each individual case, an optimal strategy has to be found by trial and error. For this reason, the LGB macro is open to variations, and the procedure is highly interactive.

Using Photoshop (Adobe Systems, 1999), an overlay of the manual tracing, the interactive tracing and the LGB derived grain boundary maps were produced. By turning the individual layers on and off, one by one, all grain boundary maps were made to coincide as well as possible by eliminating those grains near the image border that were not common to all of them. The layers are separated again and the seven grain boundary maps are subjected to the grain size analysis described above.

5. Comparison of results

For the rating of the grain boundary maps produced by the different procedures and input image sets (see Table 2, column 2 and 3), a central 600×500 area of the grain boundary maps was selected. By shifting the boundary maps a few pixels in the horizontal and/or vertical direction, an optimum match of the grain boundaries was ascertained. The outlines of each grain boundary map were selected, colour-coded and copied into seven layers of an Adobe Photoshop image, placing the manual outlines in the background layer. One by one, the outlines of sets 1–5 and the interactive ones were compared with the manual tracing. For each pair, the grey value histogram was used to determine the number of grain boundary pixels of the manual tracing that remained uncovered by the tested grain boundary map, and the total number of grain boundary pixels detected within that area. The ratio of matched to non-matched grain boundary is an indicator of the quality of the segmentation, in particular,

if the edges are detected at the correct site in the image. The ratio of matched to total grain boundary indicates the efficiency of the segmentation putting the number of detected grain boundary pixels in relation to possible oversegmentation.

5.1. Quality of grain boundary maps

The numbers of matched and non-matched grain boundary pixels are shown in column 4 and 5 of Table 2, the total number of grain boundary pixels are listed in column 6. With respect to the ratio of matched to non-matched (Table 2, column 7), image set 3 ranks before the interactive tracing with nearly equal amounts of matched and non-matched pixels. With respect to matched pixels vs. total amount of detected grain boundary (Table 2, column 8), the interactive tracing and set 3 range equally. In other words, the interactive mode and the automatic LGB procedure applied to set 3 (misorientation images) produce the best segmentations, that is, the segmentations closest to the manual tracing.

Maybe the most surprising result is the poor performance of the true orientation gradient image (set 5) which clearly ranks last with respect to segmentation quality. As has been mentioned this is due to the rather high noise level. If we consider orientation and misorientation images (i.e. CIP images), it appears that the number of images in the input set is an important factor influencing the quality of the segmentation. Set 4 (azimuth and inclination image), which consists of two images, performs better than set 5; and set 3 (three misorientation images) is better still. In the case of the photomicrographs (sets 1 and 2), the relatively high number of input images of set 1 outweighs the additional orientational information contributed to set 2 by the circular polarization image, placing set 1 before set 2.

Within the 600×500 test area, the total number of grain boundary pixels detected by manual digitization is 43554 (Table 2, column 6). Relative to this number, the interactive map and data sets 1–3 yield slightly fewer boundary pixels while data sets 4 and 5 yield slightly more. In contrast to this, the relative number of cross-sectional areas (column 9) detected in the interactive set indicate an overall undersegmentation (fewer grains), while for sets 1–5, an overall oversegmentation can be noted. In other words, the interactive map and the data sets 1–3 yield slightly shorter total grain boundary lengths and approximately the same number of grains as the manual tracing. For a constant area of evaluation, this indicates correct segmentation and possibly that the grain boundaries are slightly straighter. Data sets 4 and 5 yield increased lengths of grain boundary outline and higher numbers of grains; indicating substantial oversegmentation.

5.2. Quality of grain-size analysis

Fig. 4 shows the histograms of equivalent radii, $h(r)$, obtained by the different procedures from the different sets of input images. The histogram derived from the manual grain boundary map will be considered the 'true' data set. It shows a slightly bimodal distribution with a primary maximum between 40 and 48 μm and a secondary one between 12 and 16 μm.

This somewhat unexpected result may be the effect of the small sample size (500 grains); it is definitely not brought about by the area correction (addition of perimeter to cross-sectional area). However, it will not be discussed in any further detail here, but will simply be accepted as the data set that has to be reproduced as closely as possible by the other image sets and procedures.

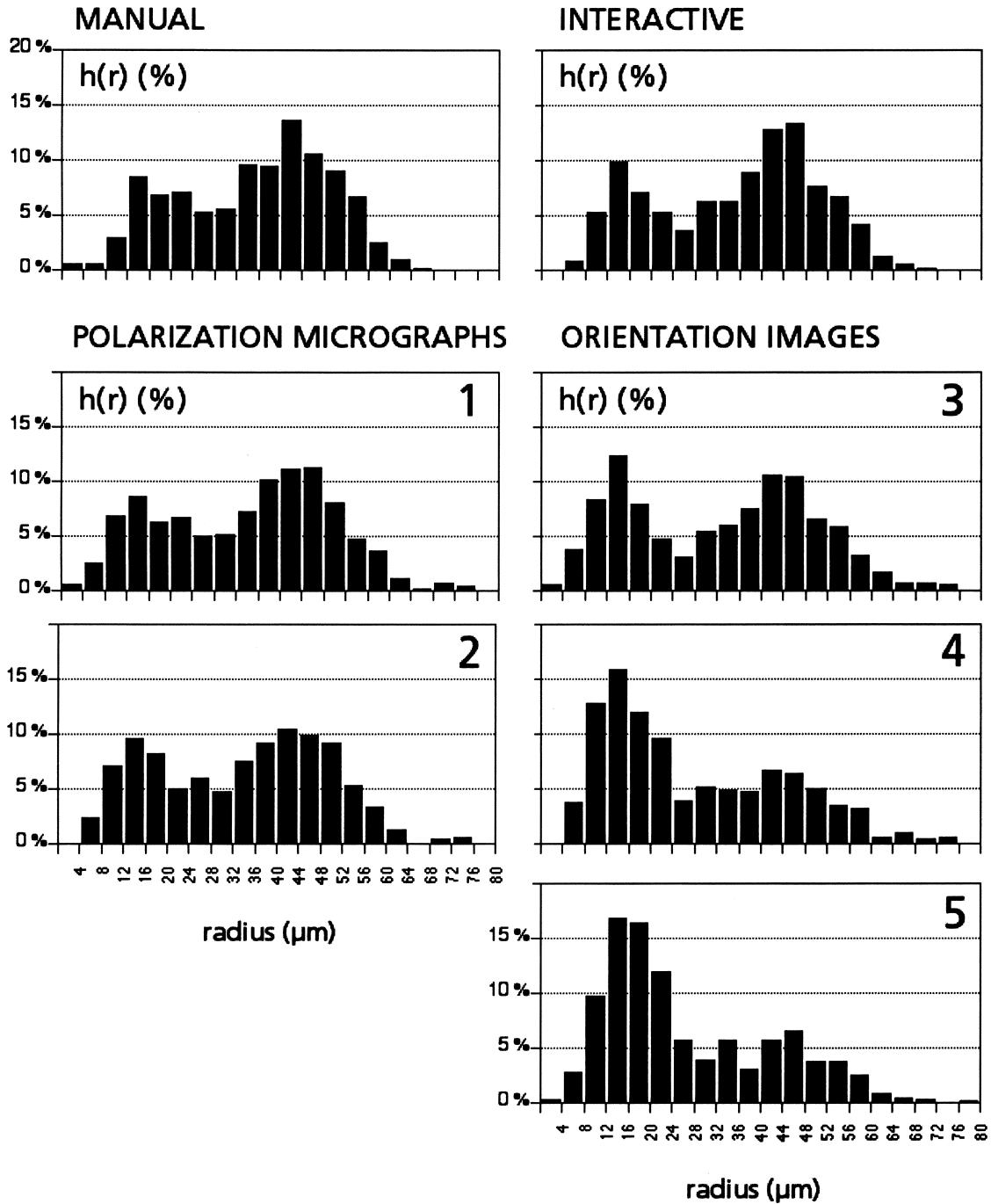The interactive procedure yields a very similar $h(r)$

Fig. 4. Histograms of 2-D grain size distributions, $h(r)$, (radii of the equivalent circles) derived from different procedures and sets of input images. Histograms are arranged as grain boundary maps in Fig. 3.

histogram; the peaks occur within exactly the same ranges (40–48 μm and 12–16 μm), and only a slight enhancement of the secondary maximum is noticeable, suggesting a slight oversegmentation. The $h(r)$ histograms of the automatically derived grain boundary maps of sets 1 and 2 (optical micrographs) show a remarkable similarity with the previous $h(r)$ histograms: the same position of the peaks in the ranges of 40–48 μm and 12–16 μm, and a slight enhancement of the secondary peak, again indicating oversegmentation. At the same time, a few extra large grains ($r > 68$ μm) indicate undersegmentation (i.e. loss of grain boundary during structural filtering). Of the CIP derived input images, set 3 yields the best coincidence with the manual $h(r)$ histogram. All sets (3–5) show a stable location of the peaks at 40–48 μm and 12–16 μm; however, from set 3–5 there is an unacceptable amount of oversegmentation, i.e. of enhancement of the lower
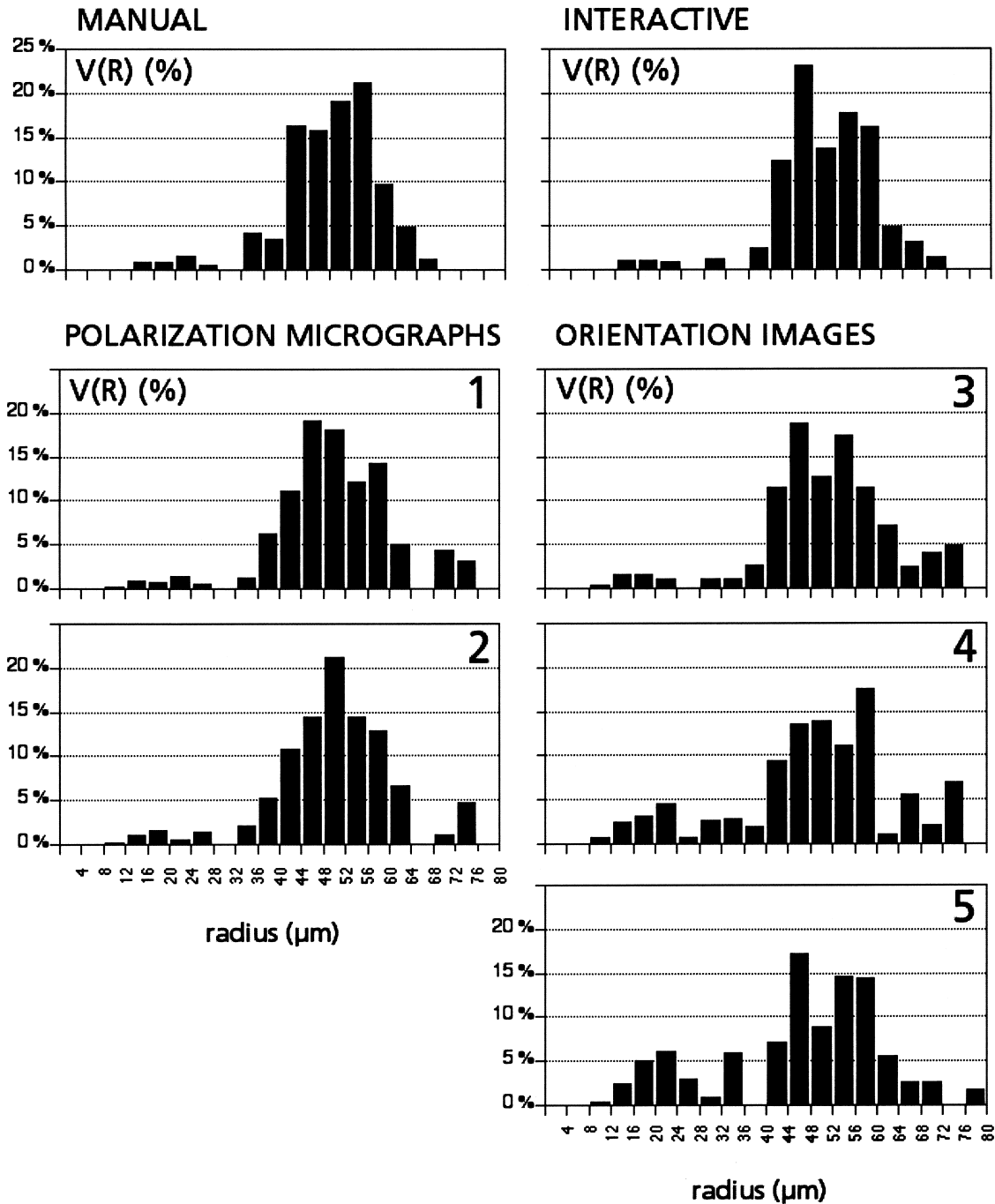

Fig. 5. Histograms of volume-weighted 3-D grain size distributions, $V(R)$, [radii of spheres calculated from the 2-D grain size distribution, $h(r)$, Fig. 4] derived from different procedures and sets of input images. Histograms are arranged as in Fig. 4 and as grain boundary maps in Fig. 3.

peak of the $h(r)$ distribution. The development of this peak remains puzzling. Since it does exist in the manual tracing, too, and since it cannot be attributed to a segmentation or area correction artefact, it is attributed to some less obvious geometric information 'concealed' in the micrographs which can be retrieved by gradient filtering.

Fig. 5 shows the volume-weighted histograms of radii of spheres, $V(R)$, calculated from the histogram $h(r)$ using the StripStar program (Heilbronner, 1998). In the course of these calculations, negative values of $V(R)$ ('antispheres') occur, providing a test of the quality of the input data (for discussion, see Heilbronner and Bruhn, 1998). The largest fraction of 'antispheres' obtained in any of the seven data sets is −0.83 vol.% for data set 5. This is a very small value, in other words, the input data sets are very good. Negative values of $V(R)$ are not shown in the histograms of Fig. 5. When comparing the $V(R)$ and the $h(r)$ histograms, two aspects are immediately obvious: firstly, the peaks are shifted to higher values of R, the mode being located in the range of 44–56 μm; secondly, contrary to the clear bimodality of the $h(r)$ distributions, the $V(R)$ histograms are practically unimodal; the secondary maximum, now in the range of 16–28 μm, is very weak.

The mean values of the $h(r)$ and the $V(R)$ distributions of the different data sets have been calculated. As is to be expected from Figs. 4 and 5, the means of $h(r)$ histograms are smaller than the means of the $V(R)$ distributions, and the means of the $V(R)$ histogram do not depend on the digitization as much as the means of the $h(r)$ histograms. The results for the manual tracing are 35 ± 14 μm for $h(r)$ and 48 ± 9 μm for $V(R)$, returning average grain sizes (diameters) of 70 μm vs. 96 μm, respectively. Calculating the means of

the $h(r)$ and $V(R)$ distributions of the other data sets and putting them in relation to the manual values (Fig. 6), we note that the $h(r)$ means drop from 100% to 75% of the manual value (for data set 5) while the $V(R)$ means stay within a range of $100 \pm 5\%$ demonstrating that the $V(R)$ histograms are more reliable estimators for the true grain size than the $h(r)$ histograms. In other words, $h(r)$ histograms tend to underestimate the average grain size and the mean values depend strongly on the quality of segmentation. In contrast, the $V(R)$ histograms are less susceptible to the details of digitization, in particular to oversegmentation, and the means of $V(R)$ represent a better estimate of the average grain size.

In terms of the number of grains detected, the interactive tracing and set 1 (six micrographs) score best, being 3% below or above the number of grains detected by the manual tracing, closely followed by set 3 (misorientation images) and 2 (four micrographs), while set 4 (azimuth and inclination image) and 5 (gradient image) are very strongly oversegmented, yielding 130% and 153%, respectively, of the number of grains of the manual tracing.

5.3. Comparison of speed

One more aspect of the quality of the different procedures is the time involved in obtaining a grain boundary map from the input images vs. the time needed to carry out a manual tracing. With respect to this aspect (Table 2, column 11), of course, the automatic procedure is best, irrespective of the input images (sets 1–4); the true gradient image (set 5) scores second because it requires extra time for preprocessing; the interactive tracing scores third, requiring one hour for 500 grains and the manual tracing is last with four hours. None of these time indications include the time required to prepare the input images.

5.4. Final ranking

The final ranking (Table 2, column 11) is obtained by adding the rankings of the grain boundary matching (column 7), efficiency (column 8), over- and undersegmentation (column 9), and speed (column 10). Based on these criteria, the automatic LGB procedure applied to an input set of three misorientation images (set 3) comes out best, followed by the interactive tracing and the automatic LGB analysis of six micrographs (set 1). There is no question that the ranking is biased, especially with respect to the weight given to the individual aspects of the ranking listed in columns 7–10 of Table 2. It is also quite obvious that any of the following factors contributes significantly to a high quality grain boundary map: (a) more time spent during the LGB analysis as, for example, in the inter-
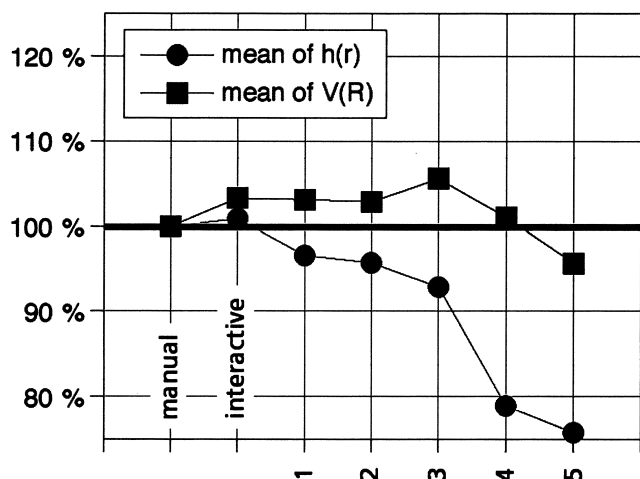

Fig. 6. Comparison of average grain sizes calculated from 2-D $h(r)$ and 3-D $V(R)$ distributions for different methods and image sets.

active case, (b) use of larger image sets as in data set 1, and (c) use of images of high information content, as in data set 3 where true angular differences with respect to three principal directions are stored.

6. Summary

- The Lazy Grain Boundary (LGB) method is a fast and easy-to-implement method for grain boundary detection; the LGB macro (for NIH Image/Scion Image) can be downloaded from the author's web site.
- The method of segmentation is a combination of gradient and structural filtering.
- The LGB method is designed to produce large grain boundary maps intended primarily for grain size analysis.
- The input consists of a set of input images; the quality and number of the input images is critical.
- The key stroke sequence for best segmentation (-> LGB macro) has to be found empirically.
- Overall, best segmentation is obtained for the automatic LGB analysis of a set of three misorientation images, for the interactive LGB analysis of the same images, and for the automatic LGB analysis of six polarization micrographs with different orientations of the polarizer–λ-plate assembly.
- The volume weighted distributions of radii of (three-dimensional) spheres, $V(R)$, are less susceptible to over- and undersegmentation than the numerical distributions of (two-dimensional) radii of sectional circles, $h(r)$; the $V(R)$ distributions represent better estimators for grain size than the $h(r)$ distributions.

References

Abelbeck Software, 1994. Kaleidagraph 3.0.5, commercial spread sheet program. http://www.synergy.com/kg.htm.

Adobe Systems, 1999. Adobe Photoshop 5.0, commercial image processing software. http://www.adobe.com/prodindex/photoshop/main.html.

Cashman, K.V., Ferry, J.M., 1988. Crystal size distribution (CSD) in rocks and the kinetics and dynamics of recrystallization. III. Metamorphic recrystallization. Contributions in Mineralogy and Petrology 99, 401–415.

Etheridge, M.A., Wilkie, J.C., 1981. An assessment of dynamically recrystallized grainsize as a paleopiezometer in quartz-bearing mylonite zones. Tectonophysics 78, 475–508.

Gonzalez, R.C., Wintz, P., 1987. Digital Image Processing. Addison-Wesley Publishing Company, Reading, Massachusetts.

Heilbronner, R., 1999. Lazy grain boundaries, public domain macros for NIH Image, University of Basel. http://www.unibas.ch/earth/GPI/micro/micro.html.

Heilbronner, R., 1998. StripStar, public domain program for the calculation of 3-D grain size distributions from histograms of 2-D sections, University of Basel. http://www.unibas.ch/earth/GPI/micro/micro.html.

Heilbronner, R., 1997. Computer-integrated polarization microscopy (CIP), public domain software for *c*-axis orientation imaging, University of Basel. http://www.unibas.ch/earth/GPI/micro/micro.html.

Heilbronner, R., Bruhn, D., 1998. The influence of three-dimensional grain size distributions on the rheology of polyphase rocks. Journal of Structural Geology 20, 695–707.

Marsh, B.D., 1988. Crystal size distribution (CSD) in rocks and the kinetics and dynamics of recrystallization. I. Theory. Contributions of Mineralogy and Petrology 99, 277–291.

National Institute of Health, 1999. NIH Image 1.62, public domain image analysis software. http://rsb.info.nih.gov/nih-image/download.html.

Panozzo Heilbronner, R., Pauli, C., 1993. Integrated spatial and orientation analysis of quartz *c*-axes by computer-aided microscopy. Journal of Structural Geology 15, 369–382.

Pettijohn, F.J., Potter, P.E., Siever, R., 1987. Sand and Sandstone. Springer-Verlag, Berlin.

Pratt, W.K., 1978. Digital Image Processing. John Wiley and Sons, New York.

Rosenfeld, A., Kak, A.C., 1976. Digital Image Processing. Academic Press, New York.

Scion Corporation, 1999. Scientific image acquisition and analysis software for Windows. http://www.scioncorp.com/.

Trimby, P.W., Prior, D.J., Wheeler, J., 1998. Grain boundary hierarchy development in a quartz mylonite. Journal of Structural Geology 20, 917.

Twiss, R.J., 1977. Theory and applicability of a recrystallized grain size paleopiezometer. Pure and Applied Geophysics 115, 227–244.

Underwood, E.E., 1970. Quantitative Stereology. Addison-Wesley, Reading, Massachusetts.